

CNN-Driven Quasiconformal Model for Large Deformation Image Registration*

Ho Law[†], Gary P. T. Choi[‡], Ka Chun Lam[§], and Lok Ming Lui[¶]

Abstract. Image registration has been widely studied over the past several decades, with numerous applications in science, engineering and medicine. Most of the conventional mathematical models for large deformation image registration rely on prescribed landmarks, which usually require tedious manual labeling and are prone to error. In recent years, there has been a surge of interest in the use of machine learning for image registration. However, most learning-based methods cannot ensure the bijectivity of the registration, which makes it difficult to establish a 1-1 correspondence between the images. In this paper, we develop a novel method for large deformation image registration by a fusion of convolutional neural network (CNN) and quasiconformal theory. More specifically, we propose a new fidelity term for incorporating the CNN features in our quasiconformal energy minimization model, which enables us to obtain meaningful registration results without prescribing any landmarks. Moreover, unlike other learning-based methods, the bijectivity of our method is guaranteed by quasiconformal theory. Experimental results are presented to demonstrate the effectiveness of the proposed method. More broadly, our work sheds light on how rigorous mathematical theories and practical machine learning approaches can be integrated for developing computational methods with improved performance.

Key words. Image registration, convolutional neural networks, quasiconformal theory

AMS subject classifications. 65D18, 68U05, 68U10, 68T07

1. Introduction. Image registration aims at establishing a meaningful correspondence between two images based on a given metric. Since the 1990s, it has been extremely useful in medical imaging, computer graphics and computer vision. For instance, one can register two medical images of a patient at different time points for disease diagnosis. One can also utilize image registration for creating animations and for tracking objects in different video frames. In particular, it is usually desirable but also more challenging to consider *non-rigid* image registrations, which involve transformations beyond simple translation, rotation and scaling.

Conventional mathematical models for non-rigid image registration can be categorized into three major types: landmark-based methods, intensity-based methods, and hybrid methods. Landmark-based methods use prescribed feature points (also known as *landmarks*) to guide the registration, while intensity-based methods use only the intensity of the images to compute the registration. Hybrid methods take the advantages of the two methods by considering both the image intensity and the landmark correspondences, which make them particularly effective for the case where the source image and the target image are assumed to be with a large deformation. However, in practice, manual landmark labeling is time-consuming and easily

*Submitted to the editors DATE.

Funding: This work was supported in part by the National Science Foundation under Grant No. DMS-2002103 (to Gary P. T. Choi), and HKRGC GRF under project ID 2130656 (to Lok Ming Lui).

[†]School of Mathematics, Georgia Institute of Technology (hlaw@gatech.edu).

[‡]Department of Mathematics, Massachusetts Institute of Technology (ptchoi@mit.edu).

[§]Machine Learning Team, National Institute of Mental Health (kachun.lam@nih.gov).

[¶]Department of Mathematics, The Chinese University of Hong Kong (lmlui@math.cuhk.edu.hk).

affected by human errors.

More recently, with the increasing popularity of machine learning, different convolutional neural networks (CNNs) have been proposed for image registration. These networks are usually trained using a large dataset of certain objects such as lung, brain or retina, so that they can compute registrations of a specific type of images effectively. However, to handle a new type of images, gathering new training sets and re-training the networks are usually necessary. Also, the bijectivity of the registration obtained using these networks is not guaranteed.

In this work, we propose a novel method for large deformation image registration by combining CNN and quasiconformal theory. Specifically, we overcome the drawback of conventional image registration methods regarding the need of manual landmark labeling, as well as the drawbacks of learning-based methods in terms of the generality of the images they can handle and the lack of bijectivity. The key idea is to establish an energy model consisting of certain regularization terms, a self-defined metric for measuring the distance between images, and a fidelity term that involves the network's output on two images. The network-based fidelity term provides us with a proper descent direction during the energy minimization process, and the regularization terms effectively correct the descent direction if the network violates the mathematical constraints we impose in terms of quasiconformality and bijectivity. Moreover, using even only a common pre-trained network, our proposed method can already work very well for images that it has not seen before.

The rest of the paper is organized as follows. In Section 2, we highlight the contributions of our work. In Section 3, we review the related works on image registration and machine learning. In Section 4, we introduce the theory of quasiconformal maps and convolutional neural networks. The proposed algorithm and the implementation are then described in Section 5 and Section 6 respectively. In Section 7, we demonstrate the effectiveness of the proposed algorithm using various experiments. We conclude the paper and discuss possible future works in Section 8.

2. Contributions. The contributions of our work are as follows:

- (i) Our proposed method combines the idea of CNN with the mathematical theory of quasiconformal maps for tackling the large deformation image registration problem. Specifically, we propose a novel fidelity term to incorporate the CNN features in our quasiconformal energy model.
- (ii) With the information given by the CNN features, the proposed method is capable of handling large deformation image registration without relying on any prescribed landmarks.
- (iii) Unlike other learning-based registration methods, the bijectivity of the proposed method is theoretically guaranteed by quasiconformal theory.
- (iv) Our work demonstrates how machine learning approaches and mathematical theories can be integrated for the development of useful computational methods.

3. Related works.

3.1. Non-rigid image registration. Over the past several decades, image registration has been extensively studied (see [1–4] for detailed surveys). In [5], Horn and Schunck presented a method for registering images using optical flow. In [6], Johnson and Christensen proposed

a method for consistent landmark and intensity-based image registration using thin-plate spline (TPS) [7]. In [8], Beg *et al.* proposed the large deformation diffeomorphic metric mapping (LDDMM) algorithm for image warping. Joshi and Miller [9] used large deformation diffeomorphisms for matching landmarks. Other publicly available image registration tools include Elastix [10], deformable image registration using discrete optimization (DROP) [11], flexible algorithms for image registration (FAIR) [12] etc.

Diffeomorphic Demons (DDemons), developed by Vercauteren *et al.* [13], is a well-known non-parametric diffeomorphic image registration method stemming from the work of Thirion [14]. By combining DDemons and quasiconformal theory, Lam and Lui [15] proposed the quasiconformal hybrid registration (QCHR) method that reduces the local geometric distortion of the registration map. The QCHR method has been successfully applied to different registration and shape analysis tasks [16, 17]. However, in case manual landmark labeling is not available and the main features in the input images do not overlap, these methods may not work well. More specifically, if there is little or no overlap of the features in the source image and the target image, these methods will only shrink the features and yield a meaningless registration map. To see this, note that the methods perform gradient descent based on the Demon force [14]:

$$(3.1) \quad u(p) = -\frac{F(p) - M \circ s(p)}{\|J^p\|^2 + \frac{\sigma_i^2(p)}{\sigma_x^2}} (J^p)^T,$$

where F is the fixed image, M is the moving image, s is the current iterated transformation, and J^p is the Jacobian of $\varphi_p^s(u) = F(p) - M \circ s \circ (Id + u)(p)$ for compositive demons. If we consider the fixed and moving images to be binary images and assume that $\text{supp}(F) \cap \text{supp}(M) = \emptyset$, i.e. the features do not overlap, then by the efficient second-order minimization (ESM) approximation $J^p = (\nabla_p^T F + \nabla_p^T (M \circ s)) / 2$, the Demon force will tend to shrink $\text{supp}(M \circ s)$. Therefore, these methods can only handle large deformation image registration with the presence of prescribed landmarks.

3.2. Image registration via machine learning. In recent years, there have been a number of works on the use of neural networks for image registration. Berendsen *et al.* [18] developed an unsupervised deep learning framework for both 2D image and 3D surface registration. However, the framework does not enforce the bijectivity of the registration. Taking bijectivity and diffeomorphic property into consideration, Balakrishnan *et al.* [19] proposed an unsupervised network called VoxelMorph, which primarily focuses on 3D object registration but can also be trained to perform atlas-based registration. Yet, the network does not necessarily produce a map with only positive Jacobian determinant as pointed out by the authors. Schmah *et al.* [20] proposed another unsupervised 3D registration learning algorithm called FAIM, which can achieve a better registration accuracy as well as a lower percentage of negative Jacobian determinants by introducing a folding penalization. However, the bijectivity of the registration is still not guaranteed.

4. Theoretical background.

4.1. Quasiconformal theory. In this work, we use quasiconformal maps to obtain diffeomorphic image registrations with large deformations. In this section, we describe some related

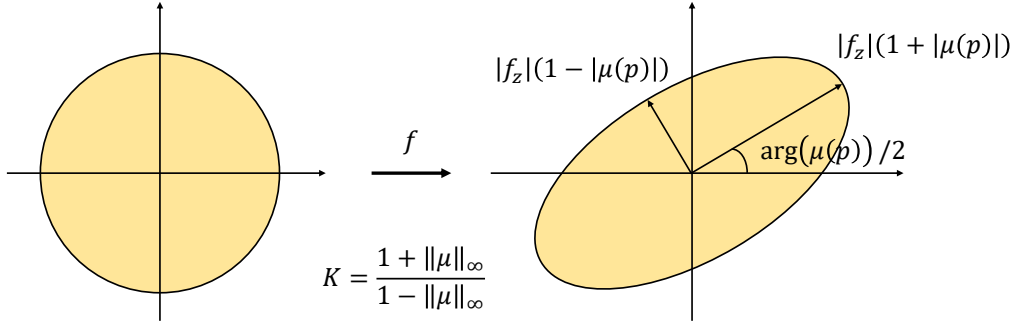


Figure 1: An illustration of how the Beltrami coefficient μ determines the conformality distortion.

concepts in quasiconformal theory. Readers are referred to [21, 22] for more details.

Let $f : \mathbb{C} \rightarrow \mathbb{C}$ be a mapping on the complex plane with $f(z) = f(x, y) = u(x, y) + iv(x, y)$, where u, v are real-valued functions. f is said to be *conformal* if it satisfies the Cauchy–Riemann equations

$$(4.1) \quad \frac{\partial u}{\partial x} = \frac{\partial v}{\partial y} \quad \text{and} \quad \frac{\partial u}{\partial y} = -\frac{\partial v}{\partial x}.$$

If we denote

$$(4.2) \quad \frac{\partial f}{\partial \bar{z}} = \frac{1}{2} \left(\frac{\partial f}{\partial x} + i \frac{\partial f}{\partial y} \right) \quad \text{and} \quad \frac{\partial f}{\partial z} = \frac{1}{2} \left(\frac{\partial f}{\partial x} - i \frac{\partial f}{\partial y} \right),$$

then Equation (4.1) can be rewritten as

$$(4.3) \quad \frac{\partial f}{\partial \bar{z}} = 0.$$

Quasiconformal maps are a generalization of conformal maps. Intuitively, the first order approximations of conformal maps take small circles to small circles, while the first order approximations of quasiconformal maps take small circles to small ellipses of bounded eccentricity [21]. Mathematically, a map $f : \mathbb{C} \rightarrow \mathbb{C}$ is said to be *quasiconformal* if it satisfies the Beltrami equation:

$$(4.4) \quad \frac{\partial f}{\partial \bar{z}} = \mu(z) \frac{\partial f}{\partial z}$$

for some complex-valued function μ (called the *Beltrami coefficient*) with $\|\mu\|_\infty < 1$. Note that μ measures how far the map at each point is deviated from a conformal map. In particular, the map f is conformal around a small neighborhood of p if and only if $\mu(p) = 0$. One may express f around a point p with respect to its local parameter as follows (see Fig. 1):

$$(4.5) \quad f(z) = f(p) + f_z(p)z + f_{\bar{z}}(p)\bar{z} = f(p) + f_z(p)(z + \mu(p)\bar{z}).$$

In other words, locally f can be considered as a map composed of a translation by $f(p)$ together with a stretch map $S(z) = z + \mu(p)\bar{z}$ with a multiplication of $f_z(p)$. Because of the factor $\mu(p)$ in $S(z)$, f maps a small circle to a small ellipse. More specifically, the maximal magnification factor is $|f_z(p)|(1 + |\mu(p)|)$ and the maximal shrinkage factor is $|f_z(p)|(1 - |\mu(p)|)$. The maximal dilation of f is then given by

$$(4.6) \quad K(f) = \frac{1 + \|\mu\|_\infty}{1 - \|\mu\|_\infty}.$$

Also, the orientation change of the major axis of the ellipse is given by $\arg(\mu(p))/2$. This shows that the Beltrami coefficient μ provides us with useful information of the quasiconformality of the mapping f .

Besides, given a Beltrami coefficient $\mu : \mathbb{C} \rightarrow \mathbb{C}$ with $\|\mu\|_\infty < 1$, there is always a quasiconformal mapping from \mathbb{C} onto itself which satisfies the Beltrami equation (4.4) in the distribution sense [21]. More precisely, we have the following theorem:

Theorem 4.1 (Measurable Riemann Mapping Theorem). *Suppose $\mu : \mathbb{C} \rightarrow \mathbb{C}$ is Lebesgue measurable and satisfies $\|\mu\|_\infty < 1$. Then there exists a quasiconformal homeomorphism ϕ from \mathbb{C} onto itself, which is in the Sobolev space $W^{1,2}(\mathbb{C})$ and satisfies the Beltrami equation (4.4) in the distribution sense. Furthermore, by fixing 0, 1 and ∞ , the quasiconformal homeomorphism ϕ is uniquely determined for any given μ .*

Theorem 4.1 suggests that under suitable normalization, a homeomorphism from \mathbb{C} onto itself can be uniquely determined by its associated Beltrami coefficient.

4.2. Linear Beltrami solver. The Linear Beltrami solver (LBS) [15] provides us with an efficient way for reconstructing a quasiconformal map $f(z) = u(x, y) + iv(x, y)$ given a Beltrami coefficient μ_f . First, note that the Beltrami equation (4.4) can be rewritten as

$$(4.7) \quad \mu_f = \frac{(u_x - v_y) + i(v_x + u_y)}{(u_x + v_y) + i(v_x - u_y)}.$$

Now, let $\mu_f(z) = \rho(z) + i\tau(z)$ where ρ, τ are real-valued functions. We can then express v_x and v_y as linear combinations of u_x and u_y :

$$(4.8) \quad \begin{aligned} -v_y &= \alpha_1 u_x + \alpha_2 u_y; \\ v_x &= \alpha_2 u_x + \alpha_3 u_y, \end{aligned}$$

where $\alpha_1 = \frac{(\rho-1)^2 + \tau^2}{1 - \rho^2 - \tau^2}$, $\alpha_2 = -\frac{2\tau}{1 - \rho^2 - \tau^2}$, and $\alpha_3 = \frac{1 + 2\rho + \rho^2 + \tau^2}{1 - \rho^2 - \tau^2}$. Similarly, we can express u_x and u_y as linear combinations of v_x and v_y :

$$(4.9) \quad \begin{aligned} u_y &= \alpha_1 v_x + \alpha_2 v_y; \\ -u_x &= \alpha_2 v_x + \alpha_3 v_y. \end{aligned}$$

Since $\nabla \cdot \begin{pmatrix} -v_y \\ v_x \end{pmatrix} = 0$ and $\nabla \cdot \begin{pmatrix} u_y \\ -u_x \end{pmatrix} = 0$, we have

$$(4.10) \quad \nabla \cdot \left(A \begin{pmatrix} u_x \\ u_y \end{pmatrix} \right) = 0 \quad \text{and} \quad \nabla \cdot \left(A \begin{pmatrix} v_x \\ v_y \end{pmatrix} \right) = 0,$$

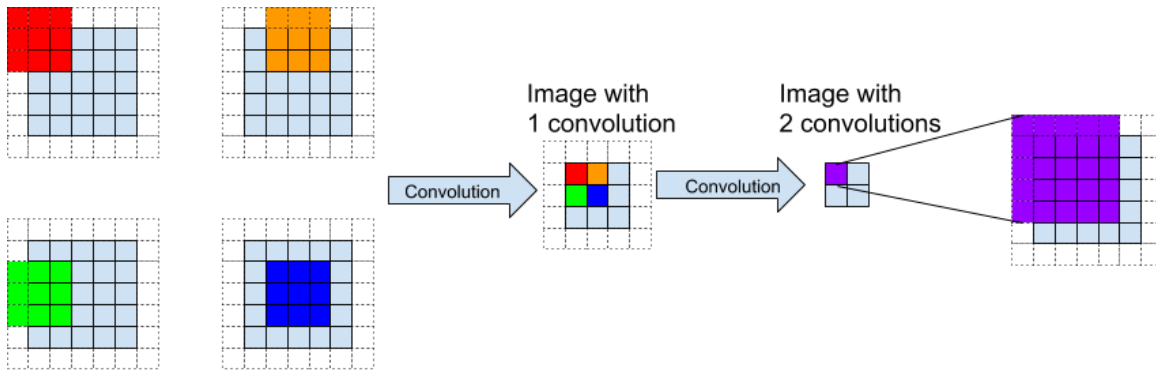


Figure 2: An illustration of receptive field.

where $A = \begin{pmatrix} \alpha_1 & \alpha_2 \\ \alpha_2 & \alpha_3 \end{pmatrix}$.

In the discrete case, the elliptic PDEs (4.10) can be discretized as sparse positive definite linear systems and hence can be efficiently solved. Readers are referred to [15, 23] for more details.

4.3. Convolutional neural networks (CNNs). Another important component in our proposed method is the use of CNNs. A comprehensive introduction to CNN can be found in [24]. Here, we introduce the concept of *receptive field* in CNN, which is particularly related to our work.

In the context of neural network for imaging, a receptive field is an area that is being read by the network at a specific layer. More specifically, the network takes in an image pixel by pixel initially and treats each pixel as a 3-dimensional vector for RGB images. Then after certain layers of convolution and pooling, the network starts to read the image region by region and it does so by assigning each region a high dimensional vector. This region is called a receptive field. In general, at the end of a CNN, the size of a receptive field would usually outgrow the size of input image, and different receptive fields overlap each other.

An illustration of receptive field is shown in Fig. 2. Suppose the input image is of size 5×5 , kernel of size 3×3 , padding of size 1 and stride of size 2×2 . After two convolutions, the purple pixels, including the padding, on the rightmost grid contribute to the value of the top left corner of the 2×2 grid. Thus, these purple pixels in the original input image form a receptive field of that top left value.

5. Proposed method. In this section, we describe our proposed CNN-driven quasiconformal method for large deformation image registration.

5.1. Measuring the correlation of image patches using a pre-trained network and receptive fields. In [25], Rocco *et al.* proposed a method for obtaining similarity information from two images using some typical image classification networks. The main idea is to extract a feature vector from each receptive field of an image using a truncated classification network, and then compute the similarities between each receptive field of the source image and the

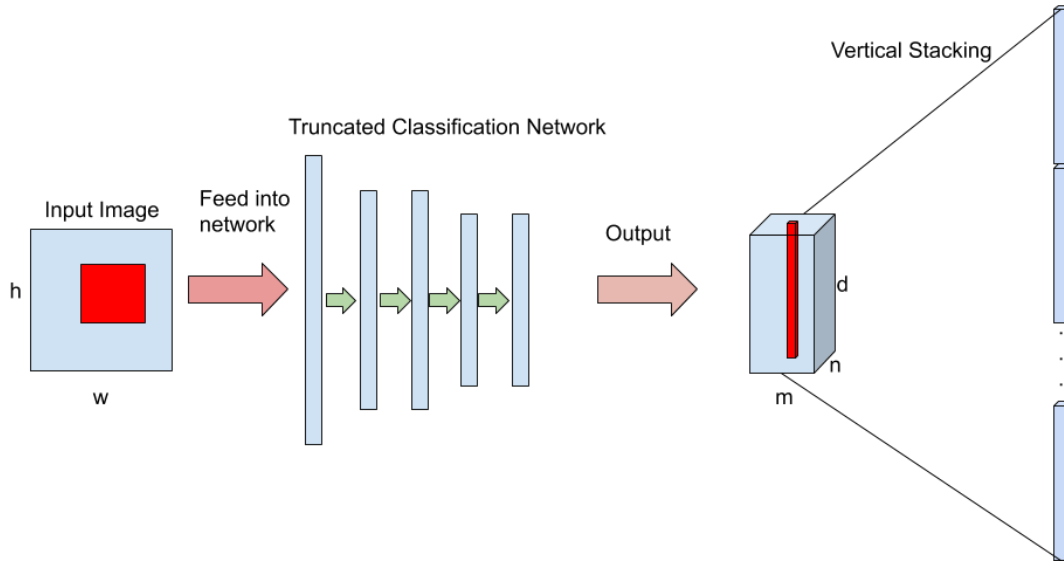


Figure 3: An illustration of stacking feature vectors.

target image using inner products. Since receptive fields are large and usually overlap with each other, this gives a way of evaluating the interaction between patches on a single image. Motivated by this approach, we partition the images using the idea in [26–30] and then evaluate the correlation of the image patches.

If we feed an image into a typical classification neural network such as ResNet [31], VGG [32] or DenseNet [33], then up to some layer in the middle, we can obtain a high dimension vector for each receptive field and stack them vertically to yield a high dimension vector. Fig. 3 illustrates the process of producing such a high dimension vector: feeding an $h \times w$ image through a truncated classification network generates a 3D array of size $m \times n \times d$, where m, n are respectively the number of receptive fields along the width and height of the input image depending on stride, kernel and padding size, and d is the dimension of the feature vector depending on the architecture of the network. Here, we remark that Fig. 3 does not reflect the actual architecture of a classification network. The red column in the cuboid represents a feature vector of the red receptive field in the input image, and for each vector we stack them up vertically. Mathematically, this stacking can be viewed as an isomorphism that maps the output array to a vector in \mathbb{R}^{mnd} . The inner product of this supreme feature vector of two images is then the sum of the correlation scores of the corresponding pairs of receptive fields. This provides us with a quantitative way for measuring the correlation of two images, which plays an important role in our proposed CNN-driven quasiconformal model described in the next section.

5.2. CNN-driven quasiconformal energy model. Let I_1 and I_2 be the moving and static images respectively. To find a diffeomorphism $f : I_1 \rightarrow I_2$ such that $\|\mu(f)\|_\infty < 1$, we propose

the following model:

$$(5.1) \quad f = \arg \min_{g: I_1 \rightarrow I_2} E_C(\mu(g)),$$

where

$$(5.2) \quad E_C(\mu) = \int_{I_1} (|\nabla \mu|^2 + \alpha |\mu|^2 + \beta (I_1 - I_2(g^\mu))^2) dz + \gamma \|C \otimes D(g^\mu) - C\|_2^2.$$

Here, α, β, γ are some positive real numbers, C is an $n \times n$ matrix, $D : \{g : I_1 \rightarrow I_2\} \rightarrow [0, 1]^{n \times n}$ maps g to an $n \times n$ matrix, and \otimes is the Hadamard product with

$$(5.3) \quad (A \otimes B)_{ij} = (A)_{ij}(B)_{ij}$$

for any matrices A, B of the same dimension. The key idea of the proposed model is to use a robust CNN to guide the registration process via the last term in the energy (5.2) while maintaining the diffeomorphic property of the deformation using the first two terms of the integral based on quasiconformal theory.

More specifically, the first term $|\nabla \mu|^2$ of the integral in the energy (5.2) is used for enhancing the smoothness of f . Recall that by Theorem 4.1, there exists a correspondence between quasiconformal mappings and the Beltrami coefficients, which measure the local geometric distortion of the mappings. Therefore, a smaller $|\nabla \mu|^2$ gives a smoother quasiconformal map f . The second term $|\mu|^2$ of the integral is used for reducing the conformality distortion of the registration. As described in Section 4, a map is conformal if and only if $\mu = 0$. A smaller $|\mu|^2$ gives a map with a lower local geometric distortion, which is desirable. The third term $(I_1 - I_2(g^\mu))^2$ of the integral aims to reduce the intensity difference of the images.

The last term $\|C \otimes D(g^\mu) - C\|_2^2$ in the proposed energy (5.2) is a novel fidelity term that gives a descent direction to help drive the whole registration based on the correlation of different regions of two images, which plays an important role in our proposed method. Below, we first introduce the definition of C and $D(g)$, and then explain the use of the Hadamard product.

Roughly speaking, the matrix C is used for deciding how trustworthy the correlation between a pair of patches is when compared with the others. To define C , we first denote $h : P \rightarrow \mathbb{R}^d$ as a truncated classification network that sends an image patch to a d -dimensional feature vector. Define a matrix $\tilde{C} \in \mathbb{R}^{n \times n}$, where n is the number of patches we partition on each image [25]:

$$(5.4) \quad (\tilde{C})_{ij} = \left\langle \frac{h(x_i^1)}{|h(x_i^1)|}, \frac{h(x_j^2)}{|h(x_j^2)|} \right\rangle.$$

It is noteworthy that passing an image patch into a truncated network would yield a 3D matrix of size $\mathbb{R}^{h \times w \times m}$, which can be viewed as \mathbb{R}^d where $d = hwm$. This allows us to define the inner product of 3D matrices as the usual inner product of vectors.

Then, we normalize each row of \tilde{C} by

$$(5.5) \quad (\hat{C})_{ij} = \frac{\tilde{C}_{ij} - \mu_i}{\sigma_i},$$

where σ_i and μ_i are the standard deviation and mean of row i respectively.

In many applications, it is common that there is a large background region with a uniform color in the images to be registered. For instance, the X-ray, CT and MRI scans in medical imaging are usually with a completely black background. For such uniform background patches in the moving image, it is expected that their corresponding rows in \hat{C} would be exactly the same and hence are not useful for the registration process. To neglect these background rows, we define an $n \times n$ elimination matrix E with

$$(5.6) \quad (E)_{ij} = \begin{cases} 0, & \text{if } i \neq j, \\ 0, & \text{if } i = j \text{ and row } i \text{ is not unique in } \hat{C}, \\ 1, & \text{if } i = j \text{ and row } i \text{ is unique in } \hat{C}. \end{cases}$$

Now, we can remove the background rows in \hat{C} and obtain an updated matrix $C^\dagger \in \mathbb{R}^{n \times n}$ by

$$(5.7) \quad C^\dagger = E\hat{C}.$$

Finally, the matrix C in the proposed energy (5.2) is constructed by sparsifying C^\dagger : For each row in C^\dagger , we keep the largest entry and set all other entries to be zero.

To define $D(g)$ in the energy (5.2), we denote the centers of image patch i and j on the moving and target images as x_i^1 and x_j^2 respectively. The mapping $D : \{g : I_1 \rightarrow I_2\} \rightarrow [0, 1]^{n \times n}$ is defined by

$$(5.8) \quad (D(g))_{ij} = \exp\left(-\frac{\|g(x_i^1) - x_j^2\|_2^2}{\sigma^2}\right),$$

where σ is a small number to be chosen.

As for the purpose of the Hadamard product in the proposed fidelity term $\|C \otimes D(g^\mu) - C\|_2^2$, note that $(D(g))_{ij} = 1$ if and only if $g(x_i^1) = x_j^2$, i.e. g maps the patch i on the moving image I_1 to the patch j on target image I_2 exactly. Now, note that the fidelity term can be expressed as a weighted sum of correspondences:

$$(5.9) \quad \|C \otimes D(g^\mu) - C\|_2^2 = \sum_{ij} C_{ij} ((D(g))_{ij} - 1)^2.$$

Therefore, with the use of the Hadamard product, $(C)_{ij}$ can serve as a weighting factor to determine how exact the mapping between x_i^1 and x_j^2 should be. More specifically, if $(C)_{ij}$ is large, i.e. the correlation between the two patches is high as determined by the pre-trained network, then $(D(g))_{ij}$ should be as close to 1 as possible; if $(C)_{ij}$ is small, the requirement for $(D(g))_{ij} = 1$ can be relaxed.

Moreover, in the optimization process, note that the proposed fidelity term can be handled using gradient descent. The descent direction $df : \{x_i^1\}_{i=1}^{n^2} \rightarrow \mathbb{R}^2$ can be explicitly written as

$$(5.10) \quad df(x_i^1) = \frac{4}{\sigma^2} \sum_j (C)_{ij} \left(\exp\left(-\frac{\|g(x_i^1) - x_j^2\|_2^2}{\sigma^2}\right) - 1 \right) (g(x_i^1) - x_j^2).$$

Therefore, if $(C)_{ij} \approx 0$, i.e. the network determines that the patch i on the moving image is not correlated to the patch j on the target image, the corresponding descent direction for the (i, j) pair will be close to 0. In other words, the Hadamard product allows us to eliminate unwanted descent directions based on the information provided by the CNN encoded in the matrix C .

On the contrary, if we replace the proposed fidelity term with $\|D(g^\mu) - C\|_2^2$, then under the same condition of $(C)_{ij} \approx 0$, the descent direction will become

$$\begin{aligned}
 df(x_i^1) &= \frac{4}{\sigma^2} \sum_j \left(\exp \left(-\frac{\|g(x_i^1) - x_j^2\|_2^2}{\sigma^2} \right) - (C)_{ij} \right) (g(x_i^1) - x_j^2) \\
 (5.11) \quad &\approx \frac{4}{\sigma^2} \sum_j \exp \left(-\frac{\|g(x_i^1) - x_j^2\|_2^2}{\sigma^2} \right) (g(x_i^1) - x_j^2) \\
 &\neq 0 \quad \text{if } g(x_i^1) \neq x_j^2.
 \end{aligned}$$

This shows that the descent direction is noisy in case the Hadamard product is not used.

After justifying our proposed energy model (5.2), it is natural to ask whether the existence of the minimizer (5.1) is guaranteed. We have the following result:

Proposition 5.1 (Existence of minimizer). *Let*

$$(5.12) \quad \mathcal{A} = \{\nu \in C^1(\omega_1) : \|D\nu\|_\infty \leq C_1; \|\nu\|_\infty \leq 1 - \epsilon\}$$

for some $C_1 > 0$ and some small $\epsilon > 0$. Then E has a minimizer in $\mathcal{A} \subset C^1(\Omega_1)$ if I_1, I_2 are L^2 functions.

Proof. From the proof of Proposition 4.1 in [15], note that \mathcal{A} is compact even without any landmark correspondences. Also, the energy (5.2) is continuous with I_1, I_2 being L^2 functions. Therefore, there exists a minimizer in \mathcal{A} . See [15] for more details. \blacksquare

As a remark, a major difference between the proposed energy model and the landmark- and intensity-based quasiconformal hybrid registration (QCHR) method [15] is that QCHR uses the prescribed feature pairs as hard landmark constraints for the energy minimization, while in our method we do not impose any landmark constraints. Using a common classification network pre-trained on very wide-ranging datasets, we obtain multiple correlated pairs of image patches. Instead of enforcing them as landmark constraints, we encode the correlation information in the proposed fidelity term in the energy (5.2), which helps supply a good descent direction for yielding a good registration. This does not only avoid any potential non-bijection due to incorrectly correlated pairs but also allow the energy model to utilize the correlation information for the registration of more general images that it has not seen before.

5.3. Energy minimization using the penalty splitting method. The penalty splitting method is used for solving the energy minimization problem (5.1). More specifically, instead of directly minimizing the energy (5.2), we minimize the following energy

$$(5.13) \quad E_C(\nu, f) = \int_{I_1} (|\nabla\nu|^2 + \alpha|\nu|^2 + \rho|\nu - \mu(f)|^2 + \beta(I_1 - I_2(f))^2) dz + \gamma\|C \otimes D(f) - C\|_2^2.$$

Here, the new term $\rho|\nu - \mu(f)|^2$ forces $\mu(f)$ to closely resemble ν . This allows us to consider the Beltrami coefficient μ and the mapping f separately, so that the optimization can be performed more easily.

Minimizing over ν . If we fix $f = f_n$, it suffices to minimize

$$(5.14) \quad E_C(\nu, f_n) = \int_{I_1} (|\nabla\nu|^2 + \alpha|\nu|^2 + \rho|\nu - \mu(f_n)|^2)dz.$$

As discussed in [15], the minimizer of the above energy can be obtained by solving the Euler–Lagrange equation:

$$(5.15) \quad (-\Delta + 2\alpha I + 2\sigma I)\nu_{n+1} = 2\sigma\mu(f_n).$$

In the discrete case, Equation (5.15) can be discretized as a sparse linear system and be solved efficiently.

Minimizing over f . If we fix $\nu = \nu_n$, it suffices to minimize

$$(5.16) \quad E_C(\nu_n, f) = \int_{I_1} (\rho|\nu_n - \mu(f)|^2 + \beta(I_1 - I_2(f))^2)dz + \gamma\|C \otimes D(f) - C\|_2^2.$$

This can be done by performing gradient descent on the Beltrami coefficient $\mu = \mu_f$ associated with f .

First, note that the descent direction for the intensity term $(I_1 - I_2(f))^2$ in the space of mappings (denoted as df_1) is given by

$$(5.17) \quad df_1 = -2(I_1 - I_2(f))\nabla I_2(f).$$

Also, the descent direction for the fidelity term $\|C \otimes D(f) - C\|_2^2$ in the space of mappings (denoted as df_2) is given by Equation (5.10):

$$(5.18) \quad df_2 = \frac{4}{\sigma^2} \sum_j (C)_{ij} \left(\exp\left(-\frac{\|g(x_i^1) - x_j^2\|_2^2}{\sigma^2}\right) - 1 \right) (g(x_i^1) - x_j^2),$$

The next step is to obtain the descent directions in the space of Beltrami coefficients (denoted as $d\mu_1$ and $d\mu_2$) from df_1 and df_2 . Note that df_1 and df_2 can be viewed as a perturbation:

$$(5.19) \quad \frac{\partial(f + df_i)}{\partial\bar{z}} = (\mu + d\mu_i) \frac{\partial(f + df_i)}{\partial z}, \quad i = 1, 2.$$

Then, following the approach in [15], we can obtain $d\mu_i$ as follows:

$$(5.20) \quad d\mu_i = \left(\frac{\partial df_i}{\partial\bar{z}} - \mu \frac{\partial df_i}{\partial z} \right) / \frac{\partial(f + df_i)}{\partial z}, \quad i = 1, 2.$$

For the term $|\nu_n - \mu(f)|^2$, the descent direction in the space of Beltrami coefficients (denoted as $d\mu_3$) is given by

$$(5.21) \quad d\mu_3 = -2(\nu_n - \mu(f)).$$

Combining the three descent directions in Equation (5.20) and Equation (5.21), we can update μ at every gradient descent iteration as follows:

$$(5.22) \quad \mu_{n+1} = \mu_n + (t_1 d\mu_1 + t_2 d\mu_2 + t_3 d\mu_3).$$

After obtaining the new μ_{n+1} , we can then reconstruct a quasiconformal map f_{n+1} associated with μ_{n+1} using the LBS method [15].

5.4. Additional intensity-based registration. In general, the input source and target images will be well registered after we perform the minimization on the energy (5.2). However, sometimes some details of the images may still not be perfectly matched. Therefore, we introduce an additional step to further improve the registration result by performing a fully intensity-based matching.

More specifically, we use the DDemons method [13] to register the current mapping result $f_n(I_1)$ and the target image I_2 , and denote the updated map as $f_n + df$. Then, we adopt the same strategy as described above to compute a descent direction $d\nu$ in the space of Beltrami coefficients. We can then obtain an updated Beltrami coefficient by

$$(5.23) \quad \nu_{n+1} = \nu_n + td\nu,$$

from which we can reconstruct a quasiconformal map f_{n+1} using the LBS method [15], with a proper truncation for enforcing that $\|\nu_{n+1}\|_\infty < 1$. We repeat the process until meeting the convergence condition.

Our proposed registration method is summarized in Algorithm 5.1.

6. Numerical implementation. In the discrete case, we discretize the input images in the form of triangular meshes. Let $V^1 = \{v_i^1\}_{i=1}^n$, $V^2 = \{v_i^2\}_{i=1}^n$ be the vertex sets and $F^1 = \{T_j^1\}_{j=1}^n$, $F^2 = \{T_j^2\}_{j=1}^n$ be the face sets of the moving image I_1 and the static image I_2 respectively.

6.1. Discretization of the Euler–Lagrange equation. The Beltrami coefficient $\mu(T)$ is first discretized on each triangular face T (see [15, 23] for details). We can then compute the Beltrami coefficient on a vertex by taking the average value of μ on its one-ring neighboring faces:

$$(6.1) \quad \mu(v_i) = \frac{1}{N_i} \sum_{T \in N_i} \mu(T),$$

where N_i is the collection of all faces incident to v_i .

The discrete Laplacian operator Δ is given by

$$(6.2) \quad \Delta(f(v_i)) = \sum_{T \in N_i} \frac{\cot \alpha_{ij} + \cot \beta_{ij}}{2} (f(v_j) - f(v_i)),$$

where α_{ij} and β_{ij} are the two angles opposite to a common edge $[v_i, v_j]$.

One can then solve the Euler–Lagrange equation (5.15) on the vertices and finally discretize the solution ν on each triangular face by taking the average value at its three vertices:

$$(6.3) \quad \nu(T) = \frac{1}{3} \sum_{v_i \in T} \nu(v_i).$$

Algorithm 5.1 CNN-driven quasiconformal image registration

Input: A moving image I_1 , a static image I_2 , a pre-trained CNN with truncation, the partition parameter m , the convergence threshold ϵ , and the maximum number of iterations n_{\max} .

Output: A quasiconformal map $f : I_1 \rightarrow I_2$.

- 1: Partition each image into m pieces.
 - 2: Pass all $2m$ pieces into the truncated network and obtain the matrix C .
CNN-driven quasiconformal energy minimization:
 - 3: Initialize $\mu_0 = 0$ and $\nu_0 = 0$.
 - 4: **while** $|\nu_{n+1} - \nu_n| > \epsilon$ and $n \leq n_{\max}$ **do**
 - 5: Fixing $f = f_n$, obtain ν_{n+1} by solving the Euler–Lagrange equation (5.15).
 - 6: Reconstruct a quasiconformal map with the Beltrami coefficient ν_{n+1} using the LBS method [15].
 - 7: Fixing $\nu = \nu_{n+1}$, obtain $\mu(f_{n+1})$ by the gradient descent method in Equation (5.22).
 - 8: Reconstruct a quasiconformal map f_{n+1} with the Beltrami coefficient μ_{n+1} using the LBS method [15].
 - 9: Update $n \leftarrow n + 1$.
 - 10: **end while**
Additional intensity-based registration:
 - 11: **while** $|\nu_{n+1} - \nu_n| > \epsilon$ and $n \leq n_{\max}$ **do**
 - 12: Use the DDemons method [13] to register $f_n(I_1)$ and I_2 and denote the mapping as $f_n + df$.
 - 13: Obtain $d\nu$ using the same procedure as in Equation (5.19) and Equation (5.20).
 - 14: Update $\nu_{n+1} \leftarrow \nu_n + td\nu$.
 - 15: Reconstruct a quasiconformal map f_{n+1} from the Beltrami coefficient ν_{n+1} using the LBS method [15], with a proper truncation to enforce $\|\nu_{n+1}\|_\infty < 1$ if necessary.
 - 16: Update $n \leftarrow n + 1$.
 - 17: **end while**
-

6.2. Numerical techniques for intensity matching. We use two different numerical optimization techniques for the intensity-based registration in the main energy minimization step and the additional intensity-matching step in Algorithm 5.1. For the main energy minimization step, we apply the modified Demon force by Wang *et al.* [34] to find the deformation:

$$(6.4) \quad u = \frac{(I_1 - I_2)\nabla I_2}{|\nabla I_2|^2 + \alpha^2(I_1 - I_2)^2} + \frac{(I_1 - I_2)\nabla I_1}{|\nabla I_1|^2 + \alpha^2(I_1 - I_2)^2}.$$

The modified Demon force is good for maintaining the diffeomorphic property of the mapping, the convergence speed as well as the stability with gradient descent. However, for the additional fully intensity-based matching step, as there can be multiple local minima for the intensity function, the gradient descent method does not necessarily yield an optimal result. Therefore, we adopt the BFGS optimization scheme [35], which takes a longer time but achieves a more accurate intensity-based registration result.

6.3. Gradient descent for the fidelity term. For the proposed data-driven fidelity term, the descent direction $df(x_i^1)$ is given by Equation (5.10). In practice, we notice that Equa-

tion (5.10) may sometimes give non-orientation preserving descent directions in some local neighborhoods, which require additional procedures of truncating the associated Beltrami coefficients and hence affect the convergence of the computation. To alleviate this issue, we apply a Gaussian smoothing on $df(x_i^1)$ around every point x_i^1 with the smoothing parameter set to be the side length of the image divided by 50.

6.4. The choice of the pre-trained network and the model parameters. In our experiment, we use a well-known CNN *DenseNet-201* [33], which is a densely connected convolutional network with 201 layers. All layers after the third dense block are truncated. The images are partitioned into $n \times n$ patches, where $n \in \{10, 12, 14, 16, 18\}$. For each registration, we consider all choices of n and choose the one that gives the best performance. Also, in practice we keep only the top 6 to 50 values of the correlation matrix C depending on the size of the features and set all other values to be 0.

As for the weighting factors in the proposed energy model (5.13), in general we set $\alpha = 5$, $\rho = 50$, $\beta = 25\rho$, and $\gamma = 5\rho$. The parameter in Equation (5.8) is set to be $\sigma = 1$.

6.5. Multiresolution scheme. To reduce the computational cost of registering high resolution images, we adopt a multiresolution scheme for the registration procedure. We first coarsen both the source image I_1 and the target image I_2 by k layers, where $I_j^0 = I_j$ is the densest image and I_j^k is the coarsest image of I_j ($j = 1, 2$). The registration process starts with registering I_1^k and I_2^k . After obtaining a diffeomorphism f_k , we proceed to a finer scale. Specifically, we obtain f_{k-1} by a linear interpolation on f_k , which serves as the initial map for the registration at the next finer layer. We repeat the above process until obtaining the registration at the finest (original resolution) layer. Using this multiresolution scheme, the computation can be significantly accelerated.

7. Experimental results. To demonstrate the effectiveness of our proposed method for large deformation image registration, we test it on various synthetic and real medical images. We remark that in all examples below, we focus on the energy at the finest (original resolution) layer of the multiresolution scheme.

7.1. Synthetic images. We first test our method on a synthetic example with the source image containing a letter ‘Z’ (Fig. 4a) and the target image containing a tilted number ‘2’ (Fig. 4b). Two major difficulties of this example are the large displacement between the ‘Z’ and the ‘2’ and the shape difference between them involving certain sharp angle changes. Although one may use an affine map to roughly align them, the boundary of the two images will be largely mismatched. As shown in Fig. 4c, our proposed registration method effectively morphs the ‘Z’ image to match the ‘2’ image. One can also visualize the registration via the deformed underlying grid as shown in Fig. 4d, from which it can be observed that the mapping is smooth and bijective. As shown in Fig. 4e, the energy decreases rapidly throughout the iterations. For comparison, we apply DDemons [13] (Fig. 4f), LDDMM [8] (Fig. 4g), Elastix [10] (Fig. 4h), and DROP [11] (Fig. 4i) for registering the images. It can be observed that all these methods fail to register the ‘Z’ and the ‘2’ shape due to the large displacement and shape change.

We then consider another synthetic example with the source image being an eagle (Fig. 5a). For the target image (Fig. 5b), we manually deform the eagle shape such that the wings are expanded wider. We apply our proposed method to obtain a registration between the two

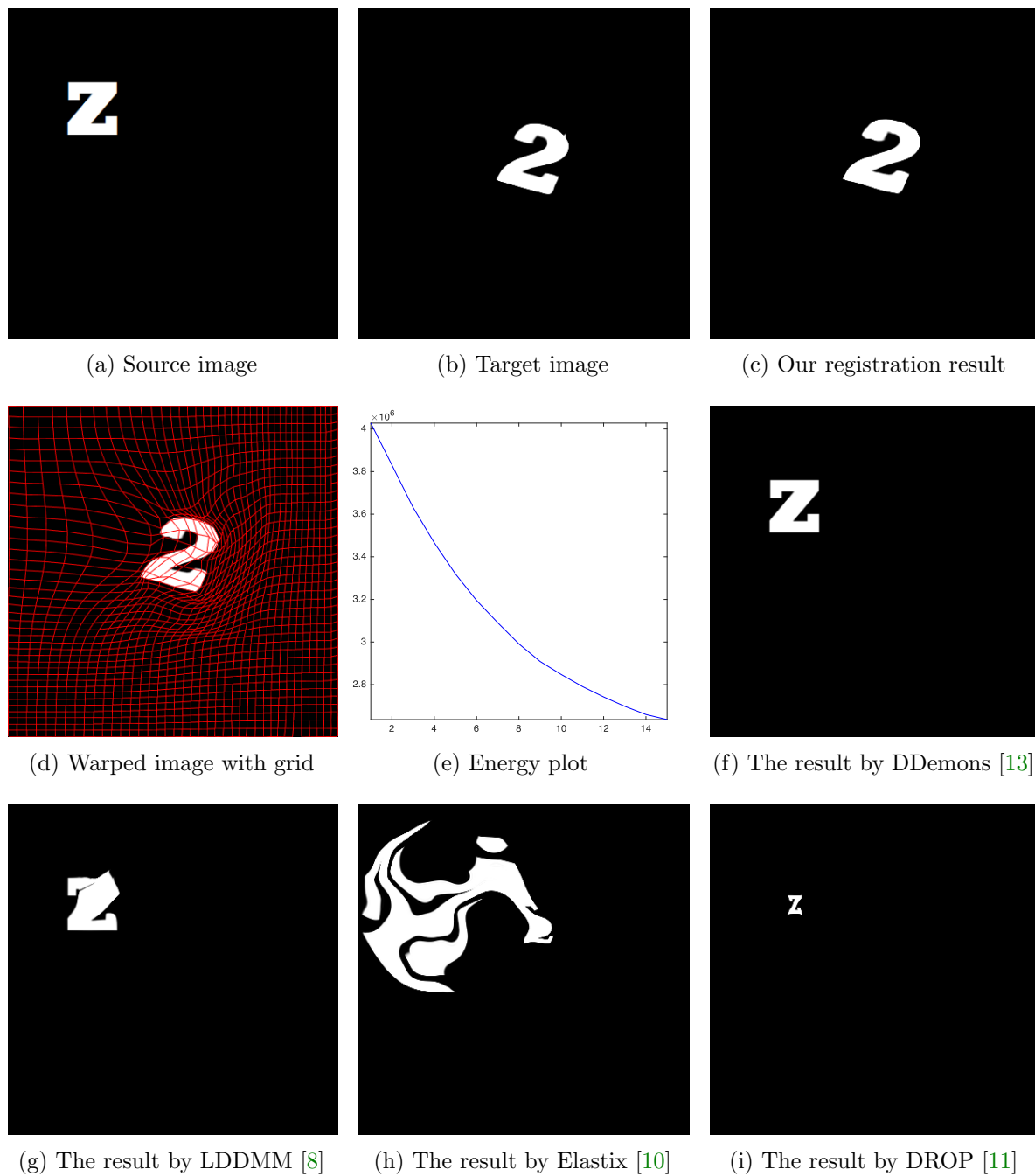


Figure 4: The ‘Z’ to ‘2’ example.

images (see Fig. 5c for the warped image and Fig. 5d for the warped image with the deformed underlying grid). Under the registration, the difference between the two images is significantly

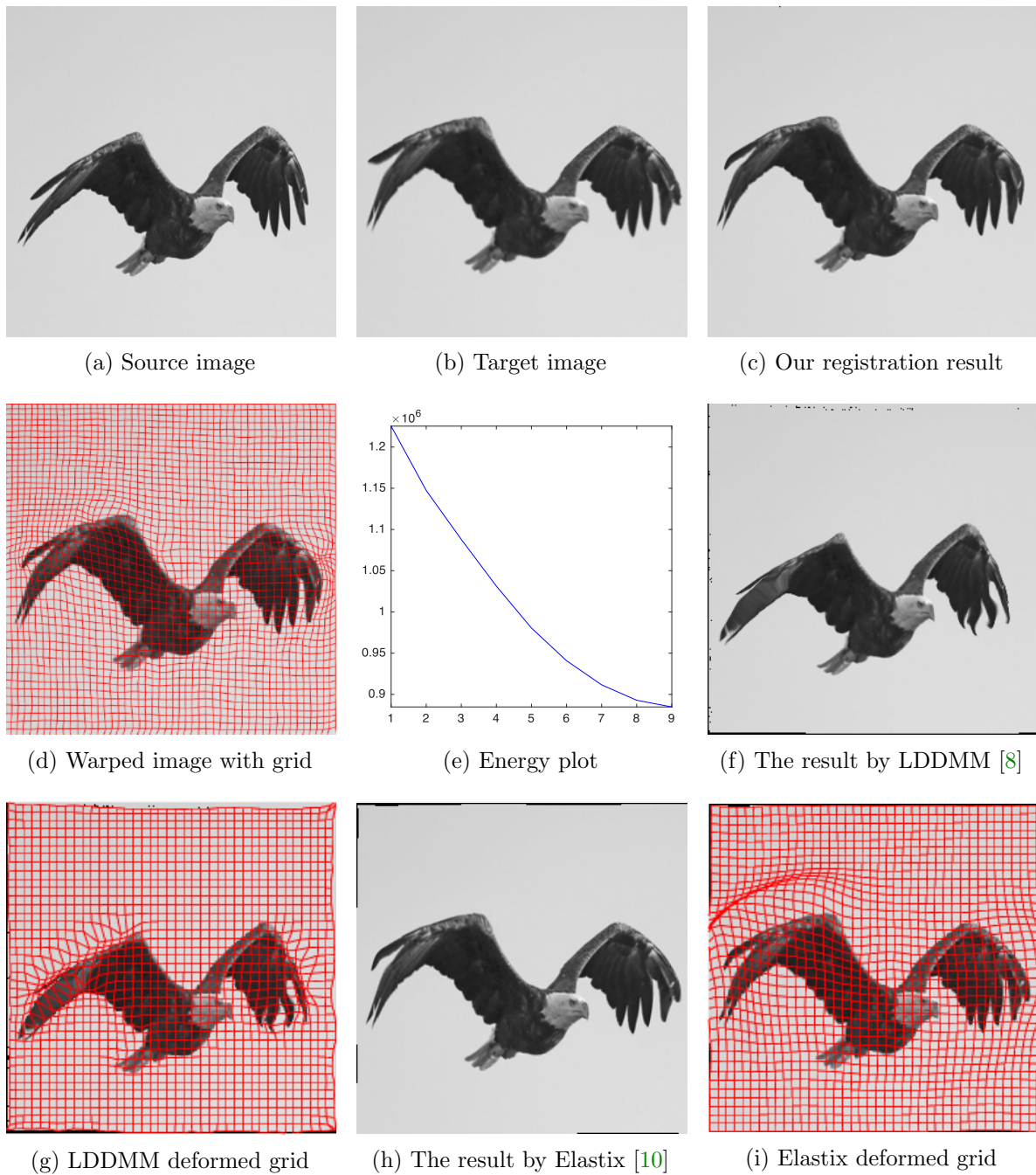


Figure 5: The eagle example.

reduced, and the energy plot in Fig. 5e again shows that our method is highly effective. On the contrary, it can be observed that LDDMM [8] does not produce an accurate registration of

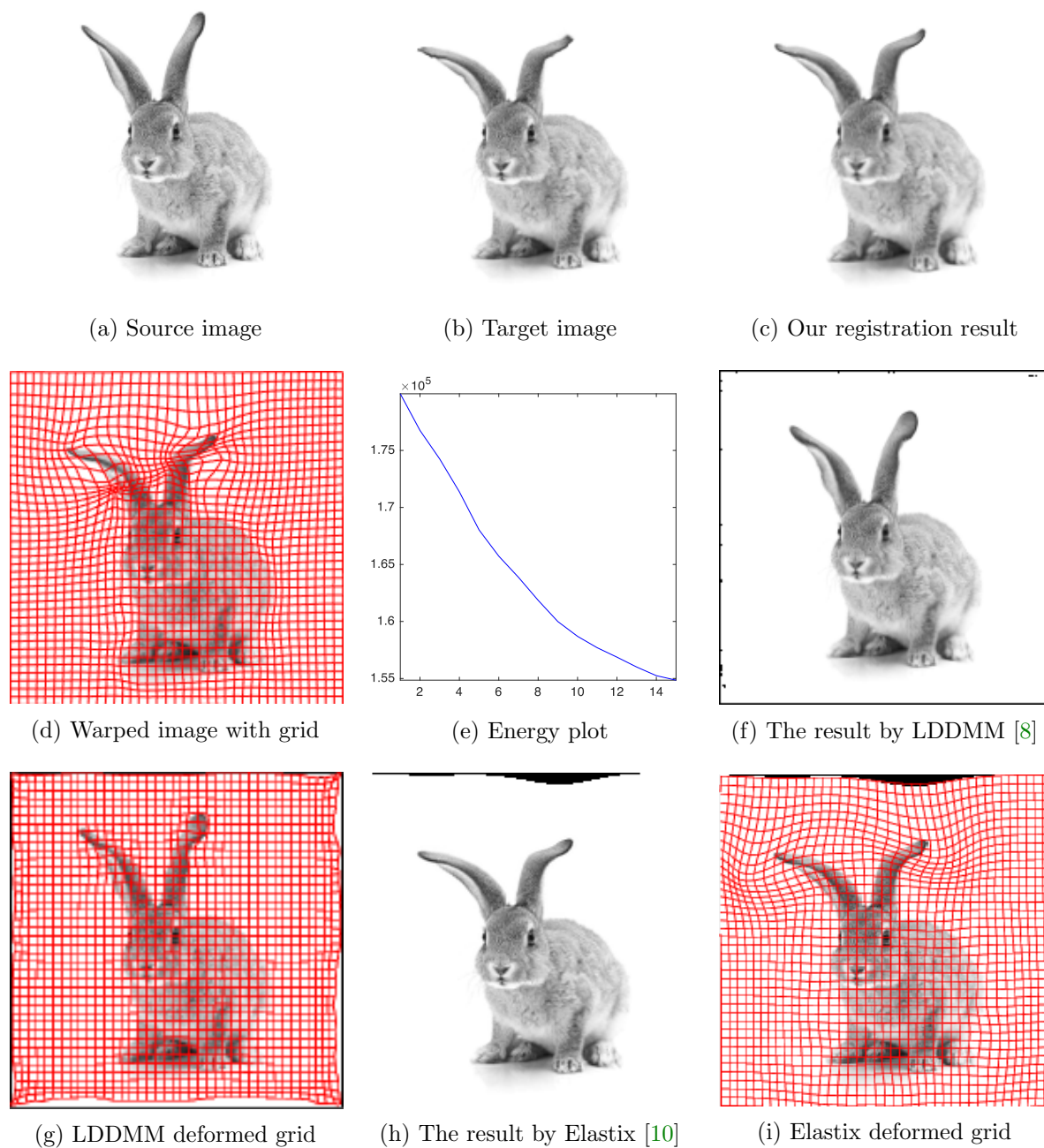


Figure 6: The rabbit example.

the wings (Fig. 5f and Fig. 5g). While the registration result by Elastix [10] looks satisfactory (Fig. 5h), there are multiple overlaps in the deformed underlying grid (Fig. 5i).

In the next example, the source image is a rabbit (Fig. 6a), and the target image is the same rabbit with its ears bent (Fig. 6b). Our method successfully morphs the ears to the desired position as shown in Fig. 6c. From the deformed underlying grid in Fig. 6d, we can see that the mapping is smooth and bijective. Also, the energy plot in Fig. 6e shows that our method effectively reduces the energy within a small number of iterations. On the contrary, LDDMM [8] fails to match the bent ears (Fig. 6f and Fig. 6g). While Elastix [10] is able to deform the ears, the overall image shape is largely distorted (Fig. 6h and Fig. 6i).

7.2. Real X-ray images. After testing our proposed method on several synthetic images, we now consider applying it on real medical images. Here, we consider a hand X-ray image as the source image (Fig. 7a) and a deformed hand X-ray image as the target image (Fig. 7b). Fig. 7c shows the original absolute intensity difference between the two images. It can be observed that different fingers are displaced in a nonuniform manner (for example, the displacement of the index finger is much larger than that of the little finger), while the wrist remains almost the same. Therefore, a simple rigid transformation is insufficient for yielding a good registration. As shown in Fig. 7d, our proposed method successfully deforms the source image to match the target image, and the final intensity difference is significantly smaller (see Fig. 7e). From the deformed underlying grid in Fig. 7f, it can be observed that the mapping is smooth and bijective. For comparison, both LDDMM [8] and DDemons [13] fail to register the fingers and are non-bijective (see Fig. 7g, Fig. 7h, and Fig. 7i).

We then consider another example of registering two hand X-ray images with larger deformations (see Fig. 8a for the source image, Fig. 8b for the target image, and Fig. 8c for their absolute intensity difference). The warped image produced by our proposed method (Fig. 8d) again closely resembles the target image with the intensity difference significantly reduced (see Fig. 8e). Fig. 8f shows that the mapping is smooth and bijective. For comparison, note that LDDMM [8] fails to match the fingers (Fig. 8g). While DROP [11] is capable of registering the fingers (Fig. 8h), it distorts the boundary shape of the overall image (Fig. 8i).

7.3. Real CT images. We now consider applying the proposed image registration method on real lung CT images retrieved from the National Lung Screening Trial (NLST) dataset [36]. Fig. 9a and Fig. 9b show two lung CT images that we use as the source and the target (see Fig. 9c for the absolute intensity difference). We remark that the CT images are originally with different intensity, and so we apply an intensity histogram matching before running the registration experiment. Fig. 9d shows the registration result obtained by our proposed method. It can be observed that our method successfully produces a large deformation on the right lung of the source image to match that of the target image (see also Fig. 9e for the final absolute intensity difference). On the contrary, DDemons [13] (Fig. 9f), LDDMM [8] (Fig. 9g), Elastix [10] (Fig. 9h) and DROP [11] (Fig. 9i) all fail to produce an accurate and bijective registration result. This shows that our method is more capable of handling large deformation image registration.

We then test our method on chest CT images obtained from the Open Access Biomedical Image Search Engine [37]. Fig. 10a shows a chest CT image from the dataset that we use as the source image. As for the target image, instead of directly using another chest CT image from the dataset, we further deform it to make the registration task more challenging (see Fig. 10b). More specifically, the dark dot at the center is manually translated to the right

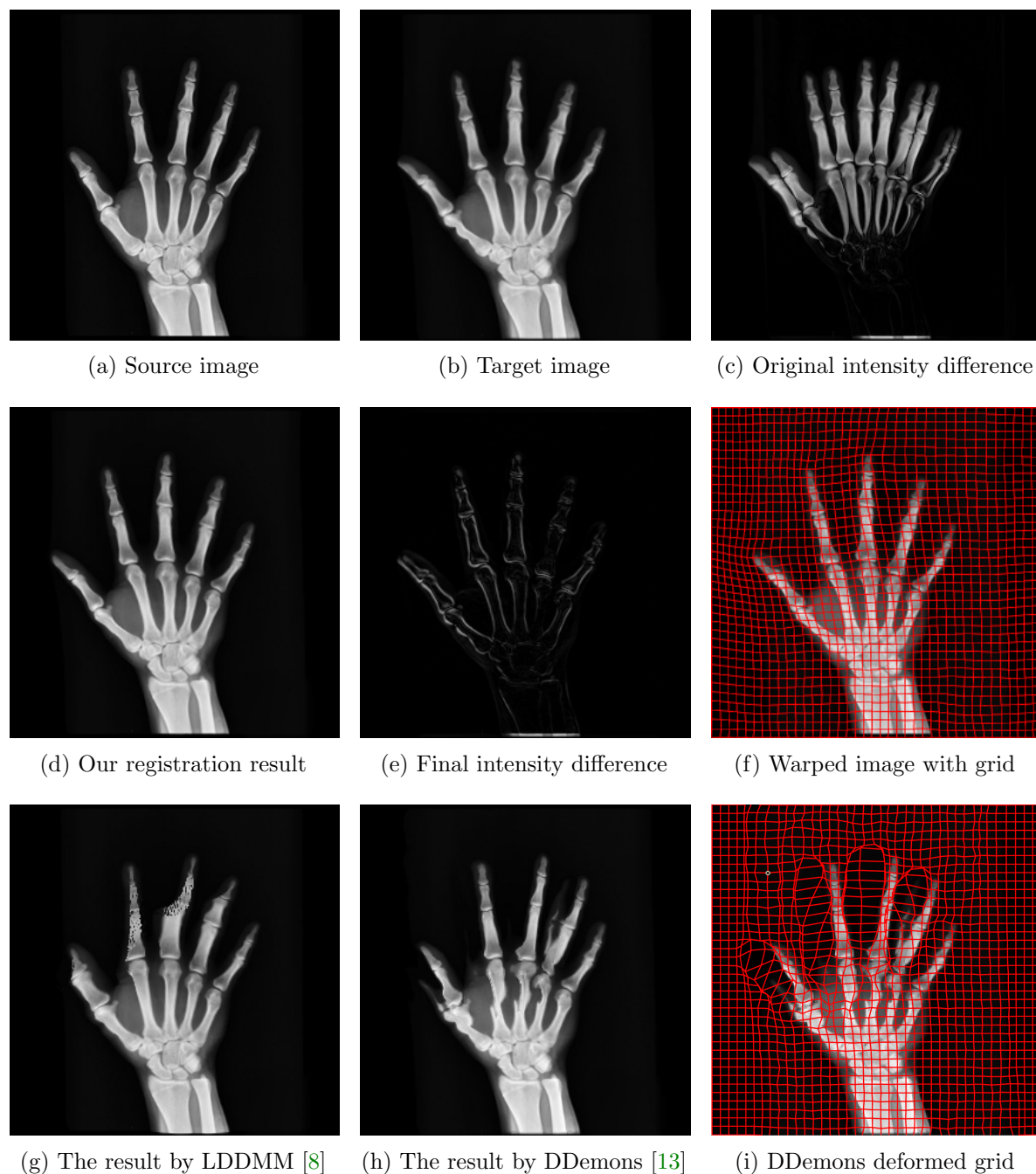


Figure 7: The first hand X-ray example.

such that the two dots in the source image and the target image do not overlap (see Fig. 10c). The registration result obtained by our proposed method is shown in Fig. 10d (see also the

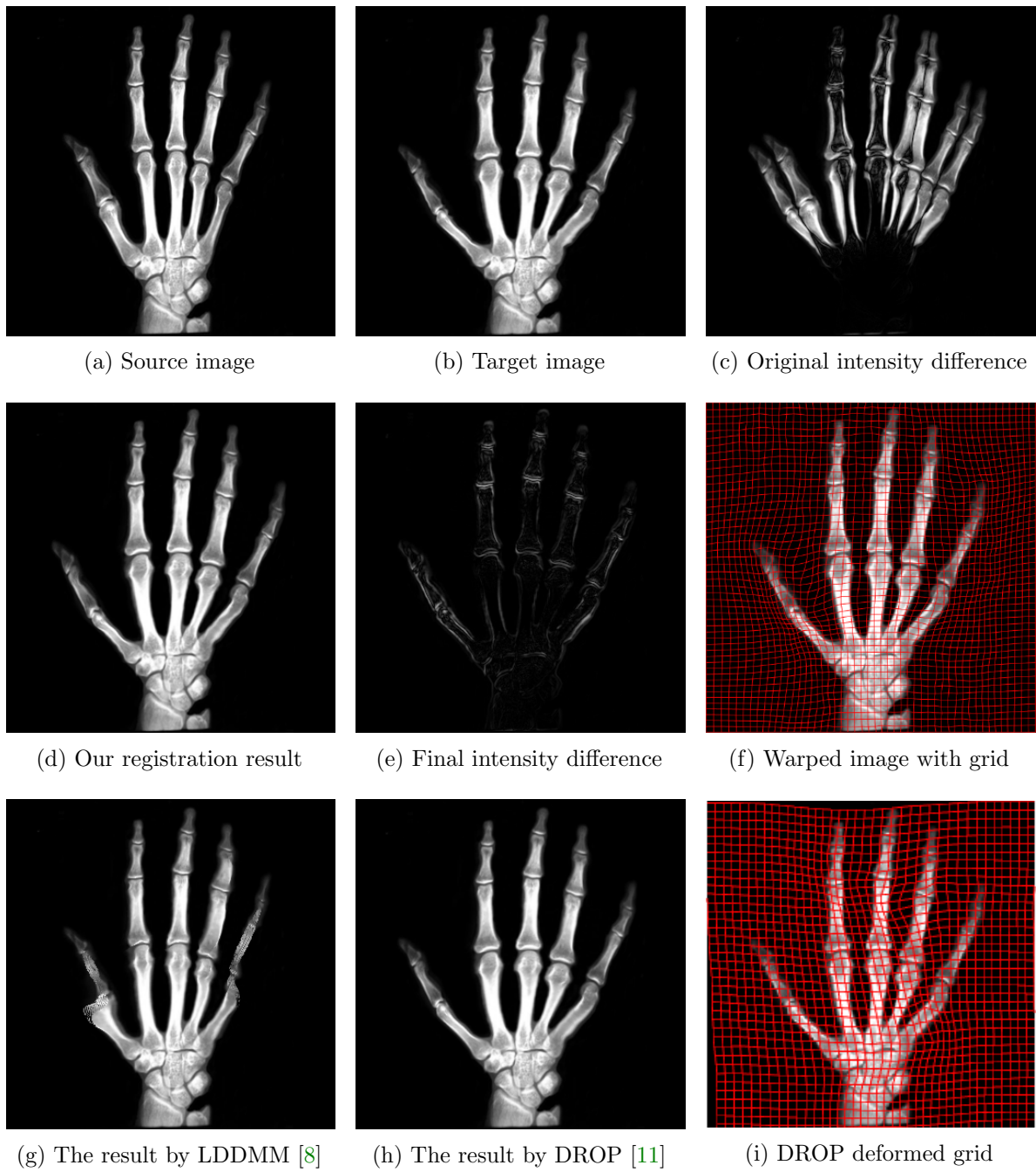


Figure 8: The second hand X-ray example.

result with the deformed underlying grid in Fig. 10e). From the final intensity difference plot in Fig. 10f, it is easily to see that our method matches not only the two large components

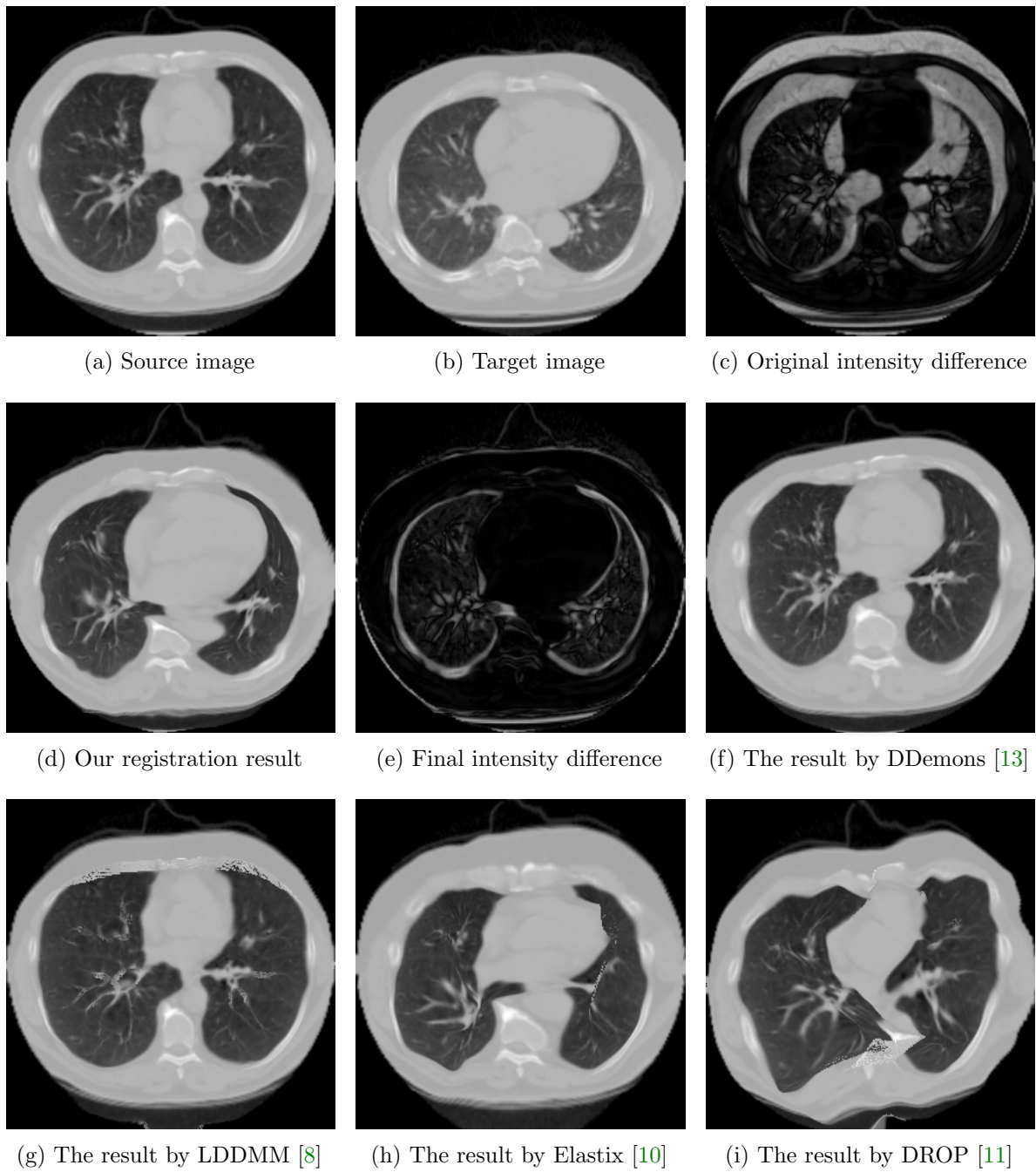


Figure 9: The lung CT example.

but also the small dot at the center very well. On the contrary, DDemons [13] produces a suboptimal registration result with a significantly larger mismatch of the small component at

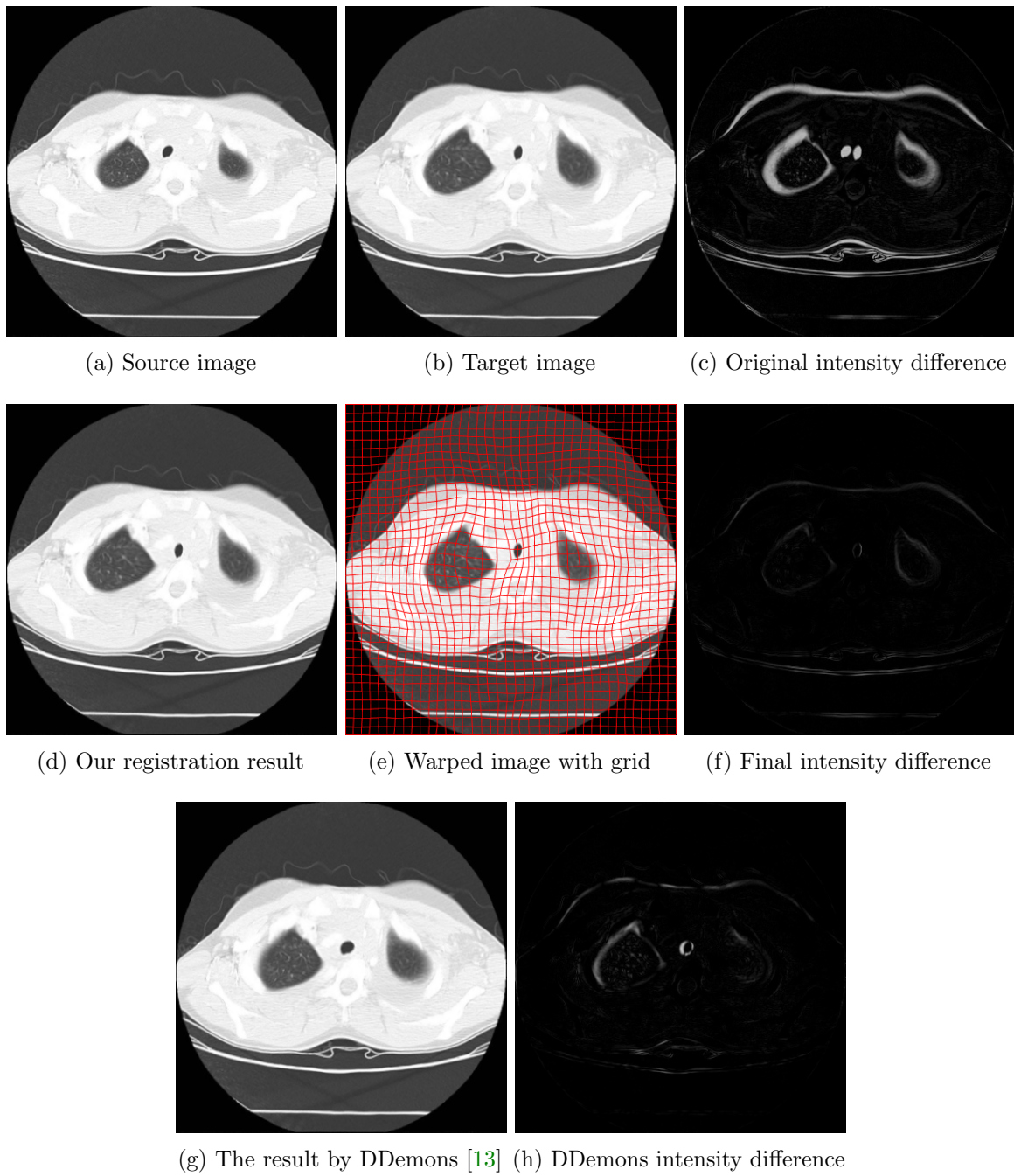


Figure 10: The chest CT example.

the center (see Fig. 10g and Fig. 10h).

7.4. Quantitative comparison between different image registration methods. For a more quantitative analysis, we compare our proposed CNN-driven quasiconformal image registration method with DDemons [13], LDDMM [8], Elastix [10], and DROP [11] in terms of the accuracy, smoothness, overall quality, and bijectivity. Here, to assess the accuracy of a registration map $f : I_1 \rightarrow I_2$, we consider the following similarity energy

$$(7.1) \quad E_{\text{sim}}(f) = \frac{\sum \sum |f(I_1) - I_2|}{2} \left(\frac{1}{\sum \sum f(I_1)} + \frac{1}{\sum \sum (1 - f(I_1))} + \frac{1}{\sum \sum I_2} + \frac{1}{\sum \sum (1 - I_2)} \right).$$

Note that $E_{\text{sim}} = 0$ if and only if $f(I_1) = I_2$, i.e. the registration matches the two images exactly. To assess the smoothness of f , we consider the following smoothness energy

$$(7.2) \quad E_{\text{smooth}}(f) = \frac{1}{mn} \sqrt{\sum \sum \left(\left(\frac{\partial f}{\partial x} \right)^2 + \left(\frac{\partial f}{\partial y} \right)^2 \right)},$$

where the size of I_1 is mn . The total energy E_{total} takes both the similarity and the smoothness into account for evaluating the overall quality of the registration:

$$(7.3) \quad E_{\text{total}} = E_{\text{sim}} + E_{\text{smooth}}.$$

Lastly, the bijectivity can be assessed by counting the number of flips in the mapping result. More specifically, we divide every image into $h \times w$ small squares evenly, and further divide each small square into 2 triangles. After applying each registration method, we count the number of triangles with the orientation flipped. A registration is bijective if and only if there is no triangle flip.

Table 1 records the performance of the above-mentioned methods. It can be observed that our method always gives a bijective registration result, while the other methods may produce flips and hence are non-bijective for various examples. Also, our method achieves the lowest total energy in general among all methods. The experiments suggest that our proposed method is more desirable for large deformation image registration.

8. Conclusion and future works. In this work, we have proposed a novel method for large deformation image registration by taking the advantage of the robustness of CNNs and the mathematical properties of quasiconformal maps. With a CNN-based fidelity term included in our proposed energy model, we are able to obtain meaningful descent directions for registering two images without imposing any landmark constraints. We also use quasiconformal theory for regularizing the CNN-driven registration process to ensure the bijectivity and reduce the local geometric distortion of the resulting mappings. Our experiments have shown that the proposed method outperforms the existing methods for the registration of both synthetic images and real medical images.

A natural next step is to consider improving the performance of the registration using a more data-specific network. Currently, the CNN features are pre-trained using a common classification network so that the proposed model can handle various types of images well. However, in many applications, the users are only interested in registering a specific type of images. For instance, ophthalmologists may only perform image registration on retina scans;

Method	Results (E_{sim} / E_{smooth} / E_{total} / # Flips)							
	'Z' to '2' (Fig. 4)	Eagle (Fig. 5)	Rabbit (Fig. 6)	Hand 1 (Fig. 7)	Hand 2 (Fig. 8)	Lung (Fig. 9)	Chest (Fig. 10)	
Our method	0.3099 0.4476 0.7575 0	0.0916 0.1558 0.2474 0	0.1953 0.1436 0.3389 0	0.1417 0.1075 0.2492 0	0.1317 0.1536 0.2853 0	0.2435 0.4774 0.7210 0	0.0368 0.1414 0.1783 0	
DDemons [13]	2.0660 0.0481 2.1141 121	0.3724 0.2470 0.6194 3697	0.1806 0.1278 0.3083 174	0.4528 0.2651 0.7180 6036	0.4273 0.2718 0.6991 8925	0.6332 0.2271 0.8602 4191	0.0725 0.3565 0.4290 16316	
LDDMM [8]	2.0488 0.2941 2.3629 105	0.3570 0.2388 0.5968 26	0.5973 0.0738 0.6711 1	0.7018 0.1842 0.8860 0	0.9563 0.1902 1.1465 6	0.6843 0.2568 0.9410 209	0.2446 0.0717 0.3164 0	
Elastix [10]	3.6377 0.9185 4.5562 68280	0.1324 0.1779 0.3103 1158	0.1808 0.1679 0.3487 0	0.1103 0.1513 0.2617 0	0.1856 0.1406 0.3263 0	0.3432 0.3203 0.6635 3579	0.0530 0.1408 0.1938 0	
DROP [11]	2.0554 0.3084 2.3638 2515	0.2509 0.1518 0.4027 0	0.1788 0.1634 0.3423 0	0.3021 0.1186 0.4207 0	1.2514 0.1406 1.3920 0	0.5065 0.6193 1.1259 3663	0.2415 0.1841 0.4256 0	

Table 1: The performance of different image registration methods for various synthetic and real medical images. Here, E_{sim} measures the accuracy of the registration mapping as described in Equation (7.1), E_{smooth} measures the smoothness of the mapping as described in Equation (7.2), E_{total} measures the overall quality of the mapping as described in Equation (7.3), and the number of flips reflects the bijectivity of the mapping.

pulmonologists may focus on registering lung scans of the patients; and neurologists may be most interested in registering brain MRI scans. By pre-training a more data-specific network, we can better include the prior information of a specific type of images and hence further improve the performance of our CNN-driven registration method for them.

Another possible future direction is to extend the proposed method for surface registration. Using conformal parameterization algorithms for meshes [38–40] or point clouds [41, 42], we can effectively flatten two 3D mesh- or point-based surfaces $\mathcal{S}_1, \mathcal{S}_2$ onto the 2D plane with low geometric distortion (denote the mappings by $\varphi_1 : \mathcal{S}_1 \rightarrow \mathbb{C}$ and $\varphi_2 : \mathcal{S}_2 \rightarrow \mathbb{C}$). Then, we can devise a similar energy minimization model for obtaining a data-driven quasiconformal map f between the flattened surfaces without imposing any landmark constraints. The composition map $\varphi_2^{-1} \circ f \circ \varphi_1$ will then give a meaningful registration between the two surfaces $\mathcal{S}_1, \mathcal{S}_2$. As manual landmark labeling is not needed, such a surface registration method may largely facilitate 3D shape morphometry [43]. This idea will be further explored and validated in our future work.

REFERENCES

- [1] L. G. Brown, “A survey of image registration techniques,” *ACM Computing Surveys (CSUR)*, vol. 24, no. 4, pp. 325–376, 1992.
- [2] J. A. Maintz and M. A. Viergever, “A survey of medical image registration,” *Medical image analysis*, vol. 2, no. 1, pp. 1–36, 1998.
- [3] B. Zitova and J. Flusser, “Image registration methods: a survey,” *Image and Vision Computing*, vol. 21, no. 11, pp. 977–1000, 2003.
- [4] A. Sotiras, C. Davatzikos, and N. Paragios, “Deformable medical image registration: A survey,” *IEEE Transactions on Medical Imaging*, vol. 32, no. 7, pp. 1153–1190, 2013.
- [5] B. K. P. Horn and B. G. Schunck, “Determining optical flow,” in *Techniques and Applications of Image Understanding*, vol. 281, pp. 319–331, International Society for Optics and Photonics, 1981.
- [6] H. J. Johnson and G. E. Christensen, “Consistent landmark and intensity-based image registration,” *IEEE Transactions on Medical Imaging*, vol. 21, no. 5, pp. 450–461, 2002.
- [7] F. L. Bookstein, “Principal warps: Thin-plate splines and the decomposition of deformations,” *IEEE*

- Transactions on Pattern Analysis and Machine Intelligence*, vol. 11, no. 6, pp. 567–585, 1989.
- [8] M. F. Beg, M. I. Miller, A. Trounev, and L. Younes, “Computing large deformation metric mappings via geodesic flows of diffeomorphisms,” *International Journal of Computer Vision*, vol. 61, no. 2, pp. 139–157, 2005.
 - [9] S. C. Joshi and M. I. Miller, “Landmark matching via large deformation diffeomorphisms,” *IEEE Transactions on Image Processing*, vol. 9, no. 8, pp. 1357–1370, 2000.
 - [10] S. Klein, M. Staring, K. Murphy, M. A. Viergever, and J. P. Pluim, “Elastix: a toolbox for intensity-based medical image registration,” *IEEE Transactions on Medical Imaging*, vol. 29, no. 1, pp. 196–205, 2009.
 - [11] B. Glocker, A. Sotiras, N. Komodakis, and N. Paragios, “Deformable medical image registration: setting the state of the art with discrete methods,” *Annual Review of Biomedical Engineering*, vol. 13, 2011.
 - [12] J. Modersitzki, *FAIR: flexible algorithms for image registration*. SIAM, 2009.
 - [13] T. Vercauteren, X. Pennec, A. Perchant, and N. Ayache, “Diffeomorphic demons: Efficient non-parametric image registration,” *NeuroImage*, vol. 45, no. 1, pp. S61–S72, 2009.
 - [14] J.-P. Thirion, “Image matching as a diffusion process: an analogy with Maxwell’s demons,” *Medical Image Analysis*, vol. 2, no. 3, pp. 243–260, 1998.
 - [15] K. C. Lam and L. M. Lui, “Landmark- and intensity-based registration with large deformations via quasi-conformal maps,” *SIAM Journal on Imaging Sciences*, vol. 7, no. 4, pp. 2364–2392, 2014.
 - [16] C. P. Yung, G. P. T. Choi, K. Chen, and L. M. Lui, “Efficient feature-based image registration by mapping sparsified surfaces,” *Journal of Visual Communication and Image Representation*, vol. 55, pp. 561–571, 2018.
 - [17] G. P. T. Choi, D. Qiu, and L. M. Lui, “Shape analysis via inconsistent surface registration,” *Proceedings of the Royal Society A*, vol. 476, no. 2242, p. 20200147, 2020.
 - [18] B. D. de Vos, F. F. Berendsen, M. A. Viergever, H. Sokooti, M. Staring, and I. Išgum, “A deep learning framework for unsupervised affine and deformable image registration,” *Medical Image Analysis*, vol. 52, pp. 128–143, 2019.
 - [19] G. Balakrishnan, A. Zhao, M. R. Sabuncu, J. Guttag, and A. V. Dalca, “VoxelMorph: A learning framework for deformable medical image registration,” *IEEE Transactions on Medical Imaging*, vol. 38, no. 8, pp. 1788–1800, 2019.
 - [20] D. Kuang and T. Schmah, “FAIM—a ConvNet method for unsupervised 3D medical image registration,” in *International Workshop on Machine Learning in Medical Imaging*, pp. 646–654, Springer, 2019.
 - [21] F. P. Gardiner and N. Lakic, *Quasiconformal Teichmüller theory*. No. 76, American Mathematical Society, 2000.
 - [22] O. Lehto and K. I. Virtanen, *Quasiconformal mappings in the plane*, vol. 126. Springer-Verlag Berlin Heidelberg, 1973.
 - [23] P. T. Choi, K. C. Lam, and L. M. Lui, “FLASH: Fast landmark aligned spherical harmonic parameterization for genus-0 closed brain surfaces,” *SIAM Journal on Imaging Sciences*, vol. 8, no. 1, pp. 67–94, 2015.
 - [24] I. Goodfellow, Y. Bengio, and A. Courville, *Deep Learning*. MIT Press, 2016. <http://www.deeplearningbook.org>.
 - [25] I. Rocco, R. Arandjelovic, and J. Sivic, “Convolutional neural network architecture for geometric matching,” in *Proceedings of the IEEE Conference on Computer Vision and Pattern Recognition*, pp. 6148–6157, 2017.
 - [26] E. Simo-Serra, E. Trulls, L. Ferraz, I. Kokkinos, P. Fua, and F. Moreno-Noguer, “Discriminative learning of deep convolutional feature point descriptors,” in *Proceedings of the IEEE International Conference on Computer Vision*, pp. 118–126, 2015.
 - [27] V. Balntas, E. Johns, L. Tang, and K. Mikolajczyk, “PN-Net: Conjoined triple deep network for learning local image descriptors,” *arXiv preprint arXiv:1601.05030*, 2016.
 - [28] X. Han, T. Leung, Y. Jia, R. Sukthankar, and A. C. Berg, “MatchNet: Unifying feature and metric learning for patch-based matching,” in *Proceedings of the IEEE Conference on Computer Vision and Pattern Recognition*, pp. 3279–3286, 2015.
 - [29] M. Jahrer, M. Grabner, and H. Bischof, “Learned local descriptors for recognition and matching,” in *Computer Vision Winter Workshop*, vol. 2, 2008.
 - [30] S. Zagoruyko and N. Komodakis, “Learning to compare image patches via convolutional neural networks,” in *Proceedings of the IEEE Conference on Computer Vision and Pattern Recognition*, pp. 4353–4361, 2015.

- [31] K. He, X. Zhang, S. Ren, and J. Sun, “Deep residual learning for image recognition,” in *Proceedings of the IEEE Conference on Computer Vision and Pattern Recognition*, pp. 770–778, 2016.
- [32] K. Simonyan and A. Zisserman, “Very deep convolutional networks for large-scale image recognition,” *Preprint arXiv:1409.1556*, 2014.
- [33] G. Huang, Z. Liu, L. Van Der Maaten, and K. Q. Weinberger, “Densely connected convolutional networks,” in *Proceedings of the IEEE Conference on Computer Vision and Pattern Recognition*, pp. 4700–4708, 2017.
- [34] H. Wang, L. Dong, J. O’Daniel, R. Mohan, A. S. Garden, K. K. Ang, D. A. Kuban, M. Bonnen, J. Y. Chang, and R. Cheung, “Validation of an accelerated ‘Demons’ algorithm for deformable image registration in radiation therapy,” *Physics in Medicine & Biology*, vol. 50, no. 12, p. 2887, 2005.
- [35] D.-J. Kroon, “Multimodality non-rigid demon algorithm image registration.” <https://www.mathworks.com/matlabcentral/fileexchange/21451-multimodality-non-rigid-demon-algorithm-image-registration>.
- [36] “The National Lung Screening Trial (NLST).” <https://cdas.cancer.gov/nlst/>.
- [37] “Open Access Biomedical Image Search Engine.” <https://openi.nlm.nih.gov/>.
- [38] P. T. Choi and L. M. Lui, “Fast disk conformal parameterization of simply-connected open surfaces,” *Journal of Scientific Computing*, vol. 65, no. 3, pp. 1065–1090, 2015.
- [39] G. P.-T. Choi and L. M. Lui, “A linear formulation for disk conformal parameterization of simply-connected open surfaces,” *Advances in Computational Mathematics*, vol. 44, no. 1, pp. 87–114, 2018.
- [40] G. P. T. Choi, Y. Leung-Liu, X. Gu, and L. M. Lui, “Parallelizable global conformal parameterization of simply-connected surfaces via partial welding,” *SIAM Journal on Imaging Sciences*, vol. 13, no. 3, pp. 1049–1083, 2020.
- [41] T. W. Meng, G. P.-T. Choi, and L. M. Lui, “TEMPO: Feature-endowed Teichmüller extremal mappings of point clouds,” *SIAM Journal on Imaging Sciences*, vol. 9, no. 4, pp. 1922–1962, 2016.
- [42] Y. Liu, G. P. T. Choi, and L. M. Lui, “Free-boundary conformal parameterization of point clouds,” *Preprint, arXiv:2010.15399*, 2020.
- [43] G. P. T. Choi, H. L. Chan, R. Yong, S. Ranjitkar, A. Brook, G. Townsend, K. Chen, and L. M. Lui, “Tooth morphometry using quasi-conformal theory,” *Pattern Recognition*, vol. 99, p. 107064, 2020.